



Article

A Robust and High-Precision Three-Step Positioning Method for an Airborne SAR Platform

Wenhao Tong, Anxi Yu *, Keke Zhang and Zhen Dong

College of Electronic Science, National University of Defense Technology (NUDT), Changsha 410073, China; twh10355@nudt.edu.cn (W.T.); zk@nudt.edu.cn (K.Z.); dongzhen@nudt.edu.cn (Z.D.)

* Correspondence: yu_anxi@nudt.edu.cn; Tel.: +86-137-8731-7450

Abstract: When airborne synthetic aperture radar (SAR) encounters long-time global navigation satellite system (GNSS) denial, the system cannot eliminate inertial navigation system (INS) accumulated drift. Platform positioning technology based on SAR image-matching is one of the important auxiliary navigation methods. This paper proposes a three-step positioning method for an airborne SAR platform, which can achieve the robust and high-precision estimation of platform position and velocity. Firstly, the motion model of the airborne SAR platform is established and a nonlinear overdetermined equation set of SAR Range-Doppler based on the ground-control points set obtained by SAR image-matching is constructed. Then, to overcome the ill-conditioned problem generated by the singular Jacobian matrix when solving the equations directly, a three-step robust and high-precision estimation of platform position and velocity is achieved through singular value decomposition and equation decoupling. Furthermore, the error transfer model of systematic and random platform positioning errors is derived. Finally, a set of semi-physical simulation experiments of airborne SAR is conducted to verify the effectiveness of the positioning method and the accuracy of the error model presented in this paper.

Keywords: SAR platform positioning; image-matching aided navigation; Gauss–Newton method; singular value decomposition; error analysis



Citation: Tong, W.; Yu, A.; Zhang, K.; Dong, Z. A Robust and High-Precision Three-Step Positioning Method for an Airborne SAR Platform. *Remote Sens.* **2023**, *15*, 3897. <https://doi.org/10.3390/rs15153897>

Academic Editor: Andrzej Stateczny

Received: 20 June 2023

Revised: 28 July 2023

Accepted: 4 August 2023

Published: 7 August 2023



Copyright: © 2023 by the authors. Licensee MDPI, Basel, Switzerland. This article is an open access article distributed under the terms and conditions of the Creative Commons Attribution (CC BY) license (<https://creativecommons.org/licenses/by/4.0/>).

1. Introduction

The airborne synthetic aperture radar (SAR) provides an important source of information that can conduct detection and reconnaissance without limitations imposed by time, weather, and environmental factors [1]. Typically, the INS/GNSS combination navigation system is used for SAR payload platforms; however, GNSS satellite signals are susceptible to interference in complex electromagnetic environments, making it difficult to obtain high-precision navigation information, and is even impossible to use in severe cases, referred to as “GNSS denial” [2]. In such an environment, the flight platform can only rely on an inertial navigation system to obtain high-precision positioning, making it challenging to conduct detection tasks [2], and even resulting in a loss of communication.

The image-matching-assisted navigation system is one of the feasible navigation solutions under GNSS denial. Using the measured map provided by the onboard high-resolution radar and comparing it with the digital map stored in the onboard computer, the geographical coordinates of several control points are obtained based on image-matching technology in the SAR image. The platform position and speed are computed according to SAR imaging geometry. This method was first applied to INS/SAR combination navigation, where positional and heading deviations are used as filter observations to correct platform position, and researchers have conducted extensive research in this area [2–5]. However, when the INS measurement is not precise enough or the platform’s position has already developed an irreducible drift, the SAR system can be used for positioning [6].

This method has been extensively researched in missile guidance. Using the distance-Doppler data of airborne SAR, the missile body’s position is estimated; INS measures

the missile's velocity and the radar altimeter measures the missile's height [7–10]. The impact of Earth curvature and rotation on the deviation is subsequently considered in the ultra-long-range, and the method is further optimized based on the characteristics of airborne SAR. The point-based approach is widely applied in missile re-entry-stage guidance; however, it cannot exploit multi-points information to conduct adjustments. Under relatively mild flight attitudes, it is not the optimal choice due to its susceptibility to errors.

For the airborne SAR scenario, research scholars have proposed the location method based on the azimuth gate, using the precise slant range at the focused azimuth moment and the geographic coordinates of the control points to conduct positioning. Referring to the cosine theorem, scholars proposed to find three control points within a single azimuth gate, and the carrier's three-dimensional position can be determined accordingly [11]. Scholars in [12–14] used the connecting line of the control points on the azimuth line to constrain the platform's position. The projection point of the platform on the horizontal plane was calculated using the slant range and altimeter to obtain the positioning of the platform at the intermediate imaging moment. However, constraining the platform's position with control points connecting lines can turn a matching error into an angular error and magnify it by distance. Scholars in [15] improved this approach by using the coarsely estimated location of each azimuth moment to accurately estimate the SAR platform's motion equation using a least-squares support vector regression.

All of the positioning methods mentioned above use the air pressure altimeter for positioning. However, the difference between the pressure altitude and the actual geographical altitude can result in significant positioning errors, and the azimuth gate positioning method inadequately utilizes Doppler information. Scholars in [16] proposed using 3D maps and flight parameters to construct simulated SAR images and compare them with real images to estimate the position by correcting flight parameters. They achieved good results. Based on the abovementioned methods, this paper proposes a robust and highly accurate three-step positioning method for an airborne SAR platform.

In Section 2, a motion model of the airborne SAR platform is established, and an equation is constructed based on the SAR scene-matching and the obtained set of ground feature points. This equation represents the nonlinear overdetermined relationship between SAR range and Doppler. During the process of solving the equations, a three-step approach is employed to achieve robust and high-precision estimations of the platform's position and velocity. This approach addresses the ill-conditioned problem caused by the singularity of the Jacobian matrix during direct solving, through techniques such as singular value decomposition and the decoupling of the equation system. Section 3 analyzes the systematic and random errors of the estimation method. In Section 4, semi-physical simulation experiments are conducted using actual SAR images and platform flight records. The influence of system parameters on estimation errors is also analyzed. Finally, a discussion and summary are provided to conclude the findings.

2. Positioning Method

2.1. Platform Positioning Model

In motion compensation for airborne SAR, the flight trajectory is often sampled and fitted as a straight line for imaging processing. The inverted flight trajectory obtained from the imaging results should also be a straight line. Therefore, a first-order polynomial with constant coefficients is used to fit the aircraft trajectory. If the coefficients can be determined, the fitted position of the platform at any time can be determined according to Equation (1). A local image coordinate system is established with the image center as the origin, the azimuth direction as the Y-axis, the range direction as the X-axis, and the elevation direction as the Z-axis. As shown in Figure 1.

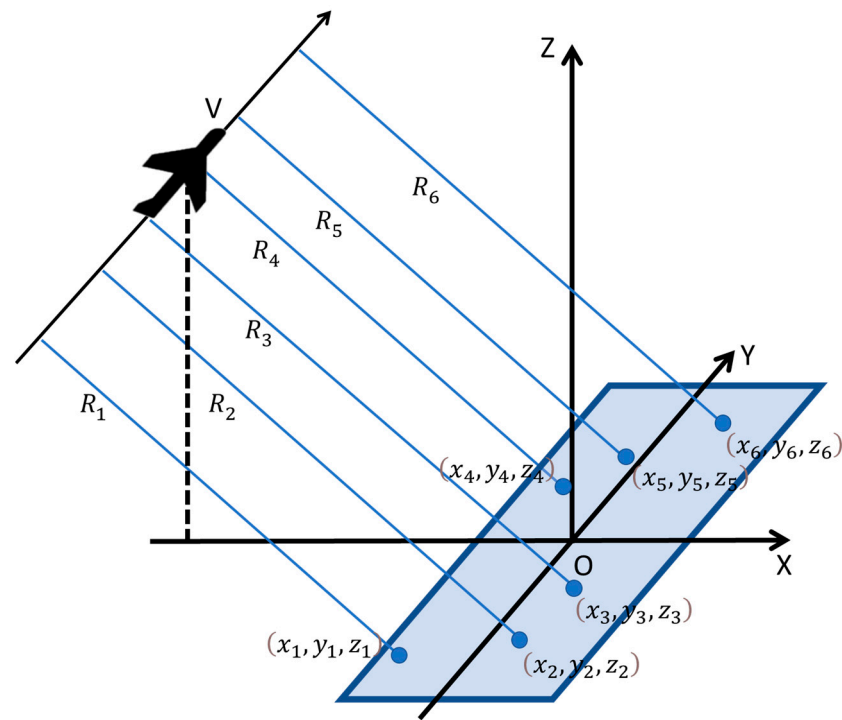


Figure 1. Local image coordinate system.

In this coordinate system, the equation of motion trajectory for the flight platform is established. This trajectory is the ideal trajectory during imaging, which is the trajectory after motion compensation.

$$\begin{cases} x(t) = x_0 + v_x t \\ y(t) = y_0 + v_y t \\ z(t) = z_0 + v_z t \end{cases} \quad (1)$$

The coordinates (x_0, y_0, z_0) represent the zero-time position in the three directions, while (v_x, v_y, v_z) represent the average velocity in the three directions, which can be rewritten as a matrix.

$$X_{\eta_i} = AT(t) \quad (2)$$

where

$$X_{\eta_i} = [x_{\eta_i} \quad y_{\eta_i} \quad z_{\eta_i}]^T, A = \begin{bmatrix} x_0 & v_x \\ y_0 & v_y \\ z_0 & v_z \end{bmatrix}, T(t) = \begin{bmatrix} 1 \\ \eta_i \end{bmatrix} \quad (3)$$

In the equation, η_i represents the zero-Doppler location of the target, i is focused after imaging, and X_{η_i} represents the coordinates of the radar at the slow time η_i .

Under the motion model of the platform, the position of each feature point in the SAR image, the radar position at the imaging time, the slant range, and the Doppler frequency all satisfy the following equation system:

$$R_i = \sqrt{(x_{\eta_i} - x_i)^2 + (y_{\eta_i} - y_i)^2 + (z_{\eta_i} - z_i)^2} \quad (4)$$

$$f_D = \frac{2}{\lambda} \frac{v_x(x_{\eta_i} - x_i) + v_y(y_{\eta_i} - y_i) + v_z(z_{\eta_i} - z_i)}{R_i} \quad (5)$$

where $(x_{\eta_i}, y_{\eta_i}, z_{\eta_i})$ represents the coordinates of the radar at the slow time η_i and (x_i, y_i, z_i) represents the coordinates of the control point X_i . R_i represents the slant range at the azimuth time of the control point and f_D represents the Doppler frequency. The coordinates of control points can be obtained through heterogeneous image-matching with optical images containing high-precision positioning information. The slant range of control

points can be obtained from focused images, while the center frequency of the Doppler can typically be obtained from the imaging processor.

Based on Equation (4), considering the errors caused by inaccurate matching, imaging, and DEM data, for any feature point $X_i(x_i, y_i, z_i)$ in the image, we have:

$$R_i + \Delta R_i = \sqrt{(x_{\eta i} - x_i)^2 + (y_{\eta i} - y_i)^2 + (z_{\eta i} - z_i)^2} \tag{6}$$

where R_i is obtained from the focused image and the ideal value of ΔR is 0. In reality, it is composed of the deviation of the matching control-point position, matching error, and slant range error. Similarly, Equation (5) has:

$$f_D + \Delta f_d = \frac{2}{\lambda} \frac{v_x(x_{\eta i} - x_i) + v_y(y_{\eta i} - y_i) + v_z(z_{\eta i} - z_i)}{R_i} \tag{7}$$

where Δf_d is composed of the estimation error of the Doppler frequency and the position error of the control points. Two equations are established for each control point. If there are n control points, the coordinates and slant range and Doppler frequency of the control points can be used to obtain a nonlinear overdetermined equation system with the number of equations being $2n$. The coefficient matrix A is estimated to minimize ΔR and Δf_d , which can be regarded as the solution of A , and then the coordinates of the radar at each time during the imaging process can be obtained. During the estimation process, we assumed that the observed measurements, including control point positions, slant ranges, and Doppler frequencies, were accurate. We iterated based on these measurements to estimate the correction amount for linear trajectory errors. However, in practical applications, these data were not entirely precise, introducing errors to the estimation results. Therefore, in Section 3, we conducted a theoretical analysis of these errors, including systematic and random components. In Section 4, we plotted error curves to visualize their characteristics.

2.2. Three-Step Solution Method

2.2.1. Gauss–Newton Iteration

According to the parameter estimation theory, the Gauss–Newton iterative method can be used to solve nonlinear over-determined equations [17]. The core idea is to locally linearize the nonlinear equations and iteratively minimize the residuals. Equation (6) can be rewritten as:

$$\begin{aligned}
 R_i + \Delta R_i &= \sqrt{(x_{\eta i} + \delta x_{\eta i} - x_i)^2 + (y_{\eta i} + \delta y_{\eta i} - y_i)^2 + (z_{\eta i} + \delta z_{\eta i} - z_i)^2} \\
 \delta x_{\eta i} &= \delta x_0 + \delta v_x \eta_i \\
 \delta y_{\eta i} &= \delta y_0 + \delta v_y \eta_i \\
 \delta z_{\eta i} &= \delta z_0 + \delta v_z \eta_i
 \end{aligned} \tag{8}$$

where $\delta x_0, \delta v_x, \delta y_0, \delta v_y, \delta z_0, \delta v_z$ is the error correction term and the unknown parameter to be estimated. The first-order expansion of Equation (8) is:

$$\Delta R_i = J_{r1} \delta x_0 + J_{r2} \delta v_x + J_{r3} \delta y_0 + J_{r4} \delta v_y + J_{r5} \delta z_0 + J_{r6} \delta v_z = J \delta A \tag{9}$$

where the coefficients are:

$$\begin{aligned}
 J_{r1} &= \frac{x_{\eta i} - x_i}{r_i} & J_{r2} &= \frac{x_{\eta i} - x_i}{r_i} \eta_i \\
 J_{r3} &= \frac{y_{\eta i} - y_i}{r_i} & J_{r4} &= \frac{y_{\eta i} - y_i}{r_i} \eta_i \\
 J_{r5} &= \frac{z_{\eta i} - z_i}{r_i} & J_{r6} &= \frac{z_{\eta i} - z_i}{r_i} \eta_i
 \end{aligned} \tag{10}$$

$$r_i = \sqrt{(x_0 + v_x \eta_i - x_i)^2 + (y_0 + v_y \eta_i - y_i)^2 + (z_0 + v_z \eta_i - z_i)^2}$$

Assuming n available feature points, these equations can be expressed in matrix form:

$$\Delta R = J_r \delta A \quad (11)$$

$$\Delta R = \begin{bmatrix} \Delta R_1 \\ \Delta R_2 \\ \dots \\ \Delta R_n \end{bmatrix}, J_r = \begin{bmatrix} J_{r1-1} & J_{r2-1} & J_{r3-1} & J_{r4-1} & J_{r5-1} & J_{r6-1} \\ J_{r1-2} & J_{r2-2} & J_{r3-2} & J_{r4-2} & J_{r5-2} & J_{r6-2} \\ \dots & \dots & \dots & \dots & \dots & \dots \\ J_{r1-n} & J_{r2-n} & J_{r3-n} & J_{r4-n} & J_{r5-n} & J_{r6-n} \end{bmatrix}, \delta A = \begin{bmatrix} \delta x_0 \\ \delta v_x \\ \delta y_0 \\ \delta v_y \\ \delta z_0 \\ \delta v_z \end{bmatrix} \quad (12)$$

The bias estimation is obtained from the least-squares principle:

$$\delta A = [J_r^T J_r]^{-1} [J_r^T \Delta R] \quad (13)$$

Utilize the estimated δA correction parameter matrix A to recalculate the Jacobian matrix and obtain a new least-squares solution. Continue to iterate until ΔR is below the threshold or the iteration limit is reached.

Similar to the slant range equation, the Doppler equation can also be rewritten and expanded as:

$$\Delta f_d = f_D - f_d = J_{f1} \delta x_0 + J_{f2} \delta v_x + J_{f3} \delta y_0 + J_{f4} \delta v_y + J_{f5} \delta z_0 + J_{f6} \delta v_z \quad (14)$$

$$\begin{aligned} J_{f1} &= \frac{2v_x}{\lambda r_i} & J_{f2} &= \frac{2(x_0 - x_i + 2v_x \eta_i)}{\lambda r_i} \\ J_{f3} &= \frac{2v_y}{\lambda r_i} & J_{f4} &= \frac{2(y_0 - y_i + 2v_y \eta_i)}{\lambda r_i} \\ J_{f5} &= \frac{2v_z}{\lambda r_i} & J_{f6} &= \frac{2(z_0 - z_i + 2v_z \eta_i)}{\lambda r_i} \end{aligned} \quad (15)$$

where f_D is the Doppler frequency obtained during the imaging process, and f_d is the Doppler frequency calculated from the position and velocity parameters. Assuming n available feature points, the equation can be expressed in matrix form:

$$\Delta f_d = J_f \delta A \quad (16)$$

The bias estimation is obtained from the least-squares principle:

$$\delta A = [J_f^T J_f]^{-1} [J_f^T \Delta f_d] \quad (17)$$

Utilize the estimated δA correction parameter matrix A to recalculate the Jacobian matrix and obtain a new least-squares solution. Continue to iterate until Δf_d is below the threshold or the iteration limit is reached.

2.2.2. Singular Value Decomposition

In the Gauss–Newton iterative method, the matrix needs to be inverted (Equations (13) and (17)); however, matrices $J_r^T J_r$ and $J_f^T J_f$ cannot ensure full rank. When the platform is imaged in a positive side view, $(y_{\eta_i} - y_i)$ in the equation tends to zero. As a result, J_{r3}, J_{r4} is approximated to be zero, indicating matrix singularity and an ill-posed equation, making it impossible to solve the equation. The singular value decomposition truncation method is used to remove the minimum singular values from the matrix [18]. Let $N = J^T J$, then N can be decomposed as:

$$N = U \Sigma V^T \quad (18)$$

where U is the eigenvector matrix of NN^T , V is the eigenvector matrix of NN^T , and Σ is the diagonal matrix composed of NN^T positive singular values. Singular values less than 10^{-2} in Σ are truncated, and Equation (13) is modified to Equation (19):

$$\delta A = [V\Sigma^{-1}U^T] [J_r^T \Delta R] \quad (19)$$

2.2.3. Three-Step Robust Solution

After the singular value decomposition removes the minimum singular values, the equation loses its estimation function for the parameters corresponding to the small singular values. When imaged in a positive side view, the parameters y_0 and v_y corresponding to J_{r3} and J_{r4} cannot be corrected and estimated. The estimation depends on other equations. In the Jacobian matrix of the Doppler equation:

$$\frac{J_{f1}}{J_{f2}} = \frac{v_x}{(x_0 - x_i + 2v_x\eta_i)} \quad (20)$$

Under the condition of a positive side view, if the platform position error is not considered:

$$x_0 - x_i = v_x\eta_i \quad (21)$$

then

$$\frac{J_{f1}}{J_{f2}} = \frac{v_x}{3v_x\eta_i} = \frac{1}{3\eta_i} \quad (22)$$

Similarly

$$\frac{J_{f1}}{J_{f2}} = \frac{J_{f3}}{J_{f4}} = \frac{J_{f5}}{J_{f6}} = \frac{1}{3\eta_i} \quad (23)$$

At this point, the Jacobian matrix components $[J_{f1} \ J_{f3} \ J_{f5}]$ and $[J_{f2} \ J_{f4} \ J_{f6}]$ are linearly dependent, that is, the matrix $J_f^T J_f$ is singular. In practice, when the platform position error is considered as a small quantity, $J_f^T J_f$ is approximately singular. Although the singular value decomposition can solve the equation singularity problem, the effect of truncating small singular values results in some platform state parameters cannot be effectively estimated.

To avoid the linear dependence problem in the Jacobian matrix of the Doppler equation, this paper proposed a robust and high-precision three-step positioning method for an airborne SAR platform. Based on the solution of the slant range equation, the method divides the unknown parameter vector of the Doppler equation into two groups, namely, position and velocity vectors, and solves them step by step to solve the singularity problem in the Jacobian matrix of the Doppler equation, and finally achieve high-precision platform positioning.

1. In the first step, the six parameters are roughly estimated by the slant range equation.

$$\Delta R_i = J_{r1}\delta x_0 + J_{r2}\delta v_x + J_{r3}\delta y_0 + J_{r4}\delta v_y + J_{r5}\delta z_0 + J_{r6}\delta v_z \quad (24)$$

$$J_r^T J_r = U_r \Sigma_r V_r^T \delta A_1 = [V_r \Sigma_r^{-1} U_r^T] [J_r^T \Delta R] \quad (25)$$

2. In the second step, the three x_0, y_0, z_0 parameters are accurately estimated by the Doppler equation, namely, the position estimation at zero time.

$$\Delta f_d = J_{f1}\delta z_0 + J_{f3}\delta y_0 + J_{f5}\delta z_0 \quad (26)$$

$$J_{f1}^T J_{f1} = U_{f1} \Sigma_{f1} V_{f1}^T \delta A_2 = [V_{f1} \Sigma_{f1}^{-1} U_{f1}^T] [J_{f1}^T \Delta f_d] \quad (27)$$

$$\delta A_1 = \begin{bmatrix} \delta x_0 \\ \delta y_0 \\ \delta z_0 \end{bmatrix}, J_{f1} = \begin{bmatrix} J_{f1-1} & J_{f3-1} & J_{f5-1} \\ J_{f1-2} & J_{f3-2} & J_{f5-2} \\ \dots & \dots & \dots \\ J_{f1-n} & J_{f3-n} & J_{f5-n} \end{bmatrix}, \Delta f_d = \begin{bmatrix} \Delta f_{d1} \\ \Delta f_{d2} \\ \dots \\ \Delta f_{dn} \end{bmatrix} \quad (28)$$

- In the third step, the three v_x, v_y, v_z parameters are accurately estimated by the Doppler equation, namely, the average velocity estimation in three directions.

$$\Delta f_d = J_{f2}\delta v_x + J_{f4}\delta v_y + J_{f6}\delta v_z \quad (29)$$

$$J_{f2}^T J_{f2} = U_{f2} \Sigma_{f2} V_{f2}^T \delta A_3 = [V_{f2} \Sigma_{f2}^{-1} U_{f2}^T] [J_{f2}^T \Delta f_{d2}] \quad (30)$$

$$\delta A_2 = \begin{bmatrix} \delta v_x \\ \delta v_y \\ \delta v_z \end{bmatrix}, J_{f2} = \begin{bmatrix} J_{f2-1} & J_{f4-1} & J_{f6-1} \\ J_{f2-2} & J_{f4-2} & J_{f6-2} \\ \dots & \dots & \dots \\ J_{f2-n} & J_{f4-n} & J_{f6-n} \end{bmatrix}, \Delta f_d = \begin{bmatrix} \Delta f_{d1} \\ \Delta f_{d2} \\ \dots \\ \Delta f_{dn} \end{bmatrix} \quad (31)$$

In all three steps, the Gauss–Newton iterative method based on singular value decomposition is used to effectively avoid the ill-posed problem of the equation. To compare the performance difference of the solution of the positioning equation before and after the decomposition of the Doppler equation, Monte-Carlo simulations were performed 1000 times using the simulation parameters in Section 4.1, and the solution errors of each step equation were statistically analyzed. The method that does not group the Doppler equation is called the two-step method. The convergence comparison of each parameter in the two- and three-step methods is shown in Figure 2, where s1, s2, and s3 represent the three-step equation-solving operations in one iteration, and s3 is ignored in the two-step method without updates.

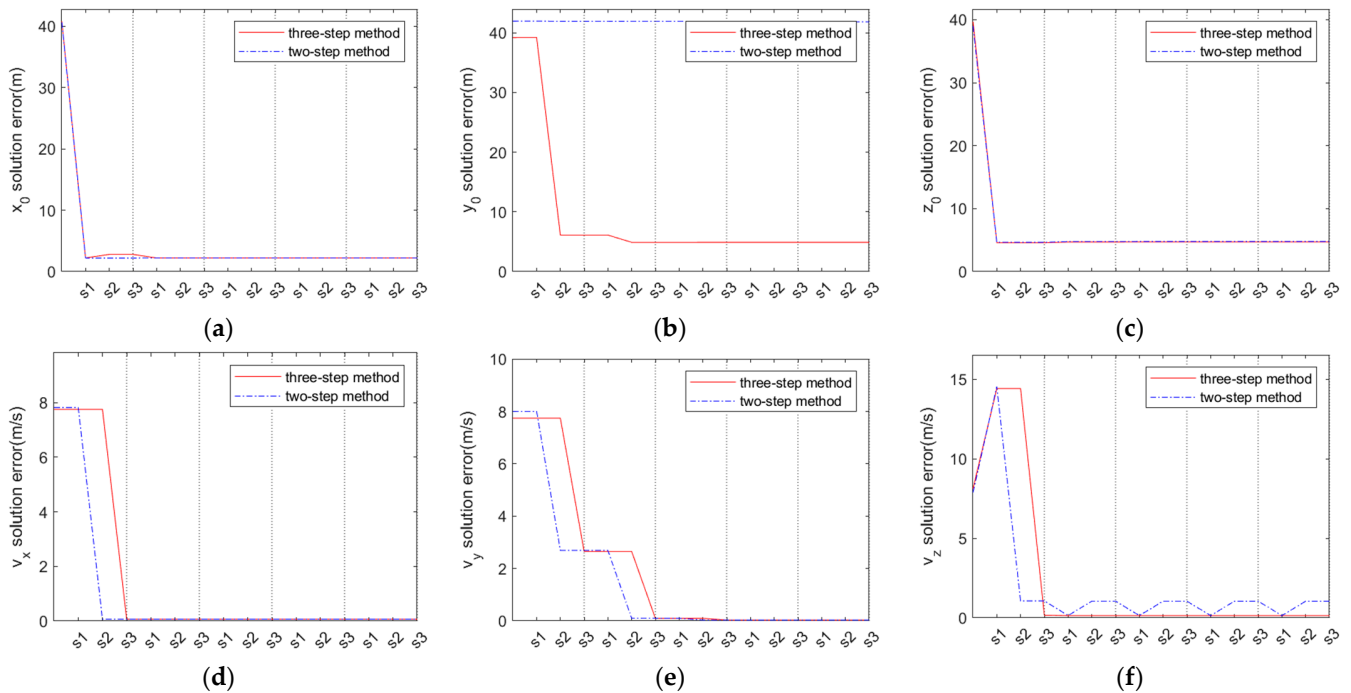


Figure 2. Convergence curves of parameter estimation errors.

From the experiments, it can be observed from subfigure (b) that the azimuth position y_0 of the platform cannot be effectively estimated using the two-step method, and the error remains consistent with the initial value, while the three-step method can rapidly

converge. From subfigure (f) the vertical velocity V_z fluctuates in the two-step method, while it stably converges in the three-step method. And from subfigures (a), (c), (d) and (e), the error convergence values of the distance and vertical position x_0, z_0 and the distance and azimuth velocity V_x, V_y obtained from the two methods are basically consistent.

3. Error Analysis

Due to the inaccuracy of the input parameters, there may be errors between the equation solving results and the actual position of the platform. These errors can be analyzed as systematic and random errors. Systematic errors are caused by the unified bias of the parameters, including the overall slant range error ΔR_t , the Doppler parameter error Δf_d , and the overall positioning offset $\Delta x_t, \Delta y_t, \Delta z_t$ of the ground-control points in three directions, which mainly affect the mean deviation of the estimation results. Random errors are caused by the random errors of the parameters, such as the random errors in the coordinates of each control point in all directions and the random errors in the imaging slant range of each point, which mainly affect the statistical variance of the estimation results.

3.1. Analysis of Systematic Errors

3.1.1. Systematic Slant Range Error

During SAR imaging, due to atmospheric refraction, receiver delay, and other reasons, there may be a fixed slant range bias ΔR in the imaging results. According to the relative position relationship between the platform and the control points in the slant range equation, the systematic slant range error produces a positional system bias in three directions according to the projection of the downward view angle and the slant view angle, it can be intuitively seen from Figure 3, and the mathematical expression is as shown in Equation (32):

$$\begin{aligned}\Delta x_p &= \sin(\theta_s) \cos(\gamma) \Delta r_t \\ \Delta y_p &= \sin(\gamma) \Delta r_t \\ \Delta z_p &= \cos(\theta_s) \cos(\gamma) \Delta r_t\end{aligned}\quad (32)$$

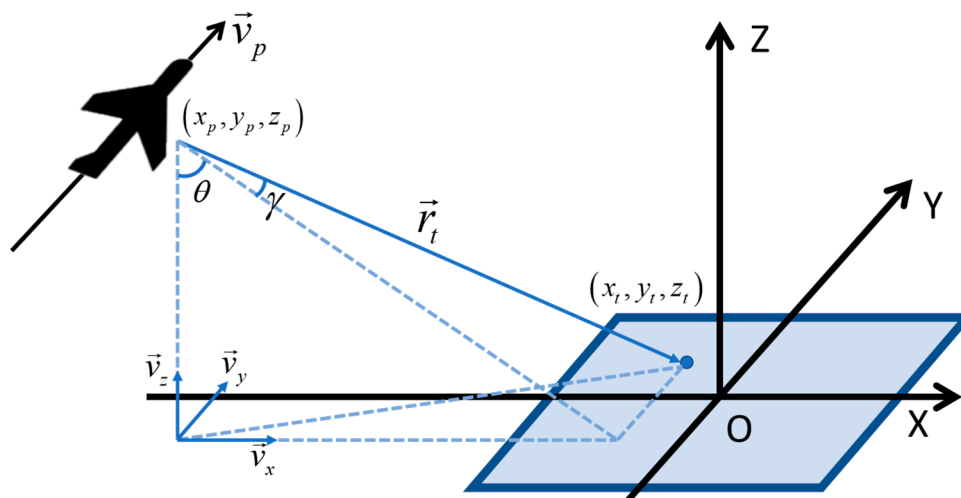


Figure 3. Projection of systematic errors.

3.1.2. Systematic Control-Point Positioning Error

Due to errors in image-matching, optical map geodetic coordinate errors, and other reasons, there may be a systematic error in the geodetic positioning coordinates of the control points compared to the true coordinates. Assuming that there is a systematic error $\Delta x_t, \Delta y_t, \Delta z_t$ in all control points in three directions, which is equivalent to translating the image coordinate system by $(-\Delta x_t, -\Delta y_t, -\Delta z_t)$, the relative relationship between the

platform positioning results and the control points remains unchanged. Therefore, a bias of $(\Delta x_t, \Delta y_t, \Delta z_t)$ also occurs in the image coordinate system, as shown in Equation (33):

$$\begin{aligned}\Delta x_p &= \Delta x_t \\ \Delta y_p &= \Delta y_t \\ \Delta z_p &= \Delta z_t\end{aligned}\quad (33)$$

3.1.3. Doppler Shift

In typical scenarios, the Doppler center frequency of control points is estimated during the imaging process and used for image-focusing. Our method intended to obtain this parameter from the imaging processor; at this point, it should be highly accurate. However, in special cases, this parameter may not be available and needs to be estimated through alternative methods. In such cases, the target Doppler center frequency we used may deviate from the true Doppler frequency; it affects the position and velocity estimations in the two-step estimation of the Doppler equation. The second-step equation is used to estimate the position, which produces position estimation errors. Expanding the vector form of the Doppler equation:

$$\Delta f_d = \frac{2|\vec{v}_p|}{\lambda} \cos\left(\frac{\pi}{2} - \gamma\right) = \frac{2|\vec{v}_p|}{\lambda} \frac{y_p - y_t}{r_t} \quad (34)$$

It can be observed that the Doppler error mainly affects y_p during the position estimation.

$$\Delta y_p = \frac{\lambda r_t}{2|\vec{v}_p|} \Delta f_d \quad (35)$$

The third-step equation was used to estimate the velocity, which produces velocity estimation errors. Assuming that $\Delta \vec{v}_{p-t}$ is the velocity error in the direction from the platform to the control points, the Doppler error can be expressed as follows:

$$\Delta f_d = \frac{2|\Delta \vec{v}_{p-t}|}{\lambda} \quad (36)$$

Decomposing $\Delta \vec{v}_{p-t}$ into three directions, we achieve:

$$\begin{aligned}\Delta v_x &= \sin \theta \cos(\gamma) |\Delta \vec{v}_{p-t}| = \frac{\lambda}{2} \sin \theta \cos(\gamma) \Delta f_d \\ \Delta v_y &= \sin \gamma |\Delta \vec{v}_{p-t}| = \frac{\lambda}{2} \sin \gamma \Delta f_d \\ \Delta v_z &= \cos \theta \cos \gamma |\Delta \vec{v}_{p-t}| = \frac{\lambda}{2} \cos \theta \cos \gamma \Delta f_d\end{aligned}\quad (37)$$

3.2. Random Error Analysis

In addition to systematic biases, the positioning coordinates of control points and the slant range at each point of the image generally exhibit varying degrees of random errors. The following analysis was conducted from the perspective of the three-step equation.

3.2.1. Error Analysis of Slant Range Equation

In the first step of solving the slant range equation, the error source ΔR was derived from two parts: the slant range random error ΔR_1 during imaging, and the slant range error ΔR_2 indirectly caused by the random error of the control points location. The two are independent.

$$cov(\Delta R) = cov(\Delta R_1) + cov(\Delta R_2) \quad (38)$$

- (1) Slant range random error ΔR_1 : assuming that the slant range random error of each control point follows an independent zero-mean Gaussian distribution $N(0, \sigma_r^2)$, I_N represents an $N \times N$ identity matrix.

$$cov(\Delta R_1) = \sigma_r^2 I_N \tag{39}$$

- (2) Random error ΔR_2 indirectly caused by control points' positioning: linearize the slant range equation for each target point coordinate.

$$\Delta R_{2_i} = \frac{x_{\eta i} - x_i}{r_i} \Delta x_i + \frac{y_{\eta i} - y_i}{r_i} \Delta y_i + \frac{z_{\eta i} - z_i}{r_i} \Delta z_i \quad i = 1, 2 \dots N \tag{40}$$

Assuming that the three-directional random error of each control point follows an independent zero-mean Gaussian distribution $N(0, \sigma_t^2)$.

$$cov(\Delta R_2) = \left(\frac{x_{\eta i} - x_i}{r_i}\right)^2 \sigma_t^2 I_N + \left(\frac{y_{\eta i} - y_i}{r_i}\right)^2 \sigma_t^2 I_N + \left(\frac{z_{\eta i} - z_i}{r_i}\right)^2 \sigma_t^2 I_N = \sigma_t^2 I_N \tag{41}$$

Combining Equations (38)–(41).

$$cov(\Delta R) = (\sigma_r^2 + \sigma_t^2) I_N \tag{42}$$

According to Equation (11) [19].

$$cov(\Delta A) = [J_r^T cov(\Delta R)^{-1} J_r]^{-1} \tag{43}$$

The estimated error of the slant range equation can be obtained:

$$cov(\Delta A) = [J_r^T (\sigma_r^2 + \sigma_t^2)^{-1} J_r]^{-1} \tag{44}$$

3.2.2. Doppler Equation Position Estimation Error Analysis

In the second step of solving the Doppler equation, the error source Δf_{d1} comes from two parts: the calculation error Δf_1 caused by inaccurate control point positioning coordinates, and the error Δf_2 indirectly introduced by the inaccurate velocity estimate in the first step of estimation. The two are mutually independent.

$$cov(\Delta f_{d1}) = cov(\Delta f_1) + cov(\Delta f_2) \tag{45}$$

Error Δf_1 indirectly caused by control points: linearize the Doppler equation for control point coordinates.

$$\Delta f_{1_i} = \frac{2V_x}{r_i \lambda} \Delta x + \frac{2V_y}{r_i \lambda} \Delta y + \frac{2V_z}{r_i \lambda} \Delta z \quad i = 1, 2, 3 \dots N \tag{46}$$

- (1) Assuming that the three-directional random error of each control point follows an independent zero-mean Gaussian distribution $N(0, \sigma_t^2)$, the error Δf_1 is as follows.

$$cov(\Delta f_1) = diag\left(\left(\frac{2}{r_i \lambda}\right)^2 (V_x^2 + V_y^2 + V_z^2) \sigma_t^2\right) \quad i = 1, 2, 3 \dots N \tag{47}$$

- (2) Error Δf_2 indirectly caused by inaccurate velocity estimates: linearize the Doppler equation for the three-directional velocity:

$$\Delta f_{2i} = \frac{2(a_0 - x_i + 2a_1 t_i)}{\lambda r_i} \Delta V_x + \frac{2(b_0 - y_i + 2b_1 t_i)}{\lambda r_i} \Delta V_y + \frac{2(c_0 - z_i + 2c_1 t_i)}{\lambda r_i} \Delta V_z \quad i = 1, 2, 3 \dots N \quad (48)$$

Simplify the coefficients for ease of expression:

$$\begin{cases} R_{xi} = \frac{2(a_0 - x_i + 2a_1 t_i)}{\lambda r_i} \\ R_{yi} = \frac{2(b_0 - y_i + 2b_1 t_i)}{\lambda r_i} \\ R_{zi} = \frac{2(c_0 - z_i + 2c_1 t_i)}{\lambda r_i} \end{cases} \quad (49)$$

Due to the correlation of velocity deviations, expand according to the covariance definition:

$$\begin{aligned} cov(\Delta f_2)_{ij} &= R_{xi} R_{xj} cov(\Delta V_x) + R_{xi} R_{yj} cov(\Delta V_x \Delta V_y) + R_{xi} R_{zj} cov(\Delta V_x \Delta V_z) \\ &\quad + R_{yi} R_{yj} cov(\Delta V_y) + R_{yi} R_{xj} cov(\Delta V_y \Delta V_x) + R_{yi} R_{zj} cov(\Delta V_y \Delta V_z) \\ &\quad + R_{zi} R_{zj} cov(\Delta V_z) + R_{zi} R_{xj} cov(\Delta V_z \Delta V_x) + R_{zi} R_{yj} cov(\Delta V_z \Delta V_y) \end{aligned} \quad (50)$$

$$i = 1, 2, 3 \dots N \quad j = 1, 2, 3 \dots N$$

The $cov(\Delta V_x), cov(\Delta V_y)$ in the equation represents the velocity estimate covariance from the first-step slant range equation error analysis. Finally, according to Equation (51), the estimate error of the Doppler equation for the position can be calculated:

$$cov(\Delta A_1) = \left[J_{f1}^T (cov(\Delta f_1) + cov(\Delta f_2))^{-1} J_{f1} \right]^{-1} \quad (51)$$

3.2.3. Doppler Equation Velocity Estimation Error Analysis

In the third step of the Doppler equation, the error source Δf_{d2} also comes from two parts: the calculation error Δf_1 caused by inaccurate control point positioning coordinates (which is the same as Equation (47)), and the error Δf_3 indirectly introduced by the inaccurate position estimate in the second step of the estimation. The two are mutually independent.

$$cov(\Delta f_{d2}) = cov(\Delta f_1) + cov(\Delta f_3) \quad (52)$$

Linearize the platform position parameters for the first order:

$$\Delta f_{3i} = \frac{2V_x}{r_i \lambda} \Delta x_p + \frac{2V_y}{r_i \lambda} \Delta y_p + \frac{2V_z}{r_i \lambda} \Delta z_p \quad i = 1, 2 \dots N \quad (53)$$

The covariance expression is as follows:

$$cov(\Delta f_3)_{ij} = \frac{4(V_y^2 \sigma_{px}^2 + V_y^2 \sigma_{py}^2 + V_y^2 \sigma_{pz}^2)}{r_i r_j \lambda^2} \quad i = 1, 2 \dots N \quad j = 1, 2 \dots N \quad (54)$$

Finally, according to Equation (55), the estimate error of the Doppler equation for the velocity can be calculated:

$$cov(\Delta A_2) = \left[J_{f2}^T (cov(\Delta f_1) + cov(\Delta f_3))^{-1} J_{f2} \right]^{-1} \quad (55)$$

In summary, since both the slant range equation and the Doppler equation estimate all six parameters, each of the three-step equations produce their own estimate errors, and the final estimate error depends on the smallest of the two values:

$$\begin{aligned}
 \sigma_{x0}^2 &= \min(\text{cov}(\Delta A)_{11}, \text{cov}(\Delta A_1)_{11}) \\
 \sigma_{y0}^2 &= \min(\text{cov}(\Delta A)_{33}, \text{cov}(\Delta A_1)_{22}) \\
 \sigma_{z0}^2 &= \min(\text{cov}(\Delta A)_{55}, \text{cov}(\Delta A_1)_{33}) \\
 \sigma_{vx}^2 &= \min(\text{cov}(\Delta A)_{22}, \text{cov}(\Delta A_2)_{11}) \\
 \sigma_{vy}^2 &= \min(\text{cov}(\Delta A)_{44}, \text{cov}(\Delta A_2)_{22}) \\
 \sigma_{vz}^2 &= \min(\text{cov}(\Delta A)_{66}, \text{cov}(\Delta A_2)_{33})
 \end{aligned}
 \tag{56}$$

4. Results

4.1. Error Propagation Curve

A simulation experiment was designed to conduct a single-factor analysis of various errors and observe the impact of various errors on the parameters of SAR platform motion in the nadir and side-looking modes. The system parameters are shown in Table 1. The control points were uniformly selected at 200 m intervals in the imaging area. Figure 4 shows the diagram.

Table 1. Simulation system parameters.

Parameters	Value
Flight altitude of platform	8000 m
Center distance	15,000 m
Flight speed	200 m/s
Imaging area	3.6 × 2.4 km
Number of control points	247

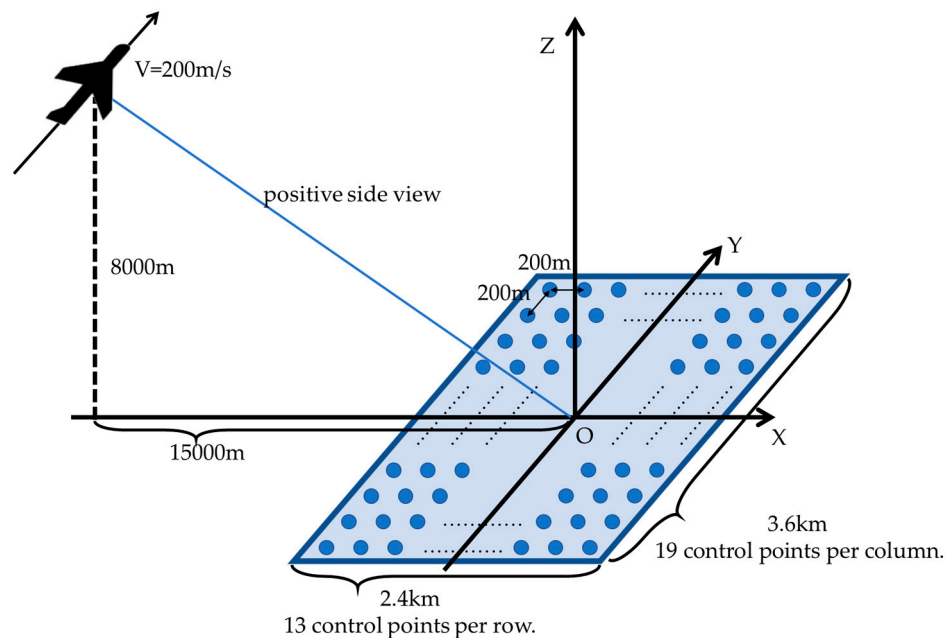


Figure 4. Scenarios of simulation experiment.

Figures 5–7 show the error propagation curve of systematic errors. The solid line represents the position estimation error and the dashed line represents the velocity estimation error. The red, green, and blue colors represent the x , y , z directions, respectively.

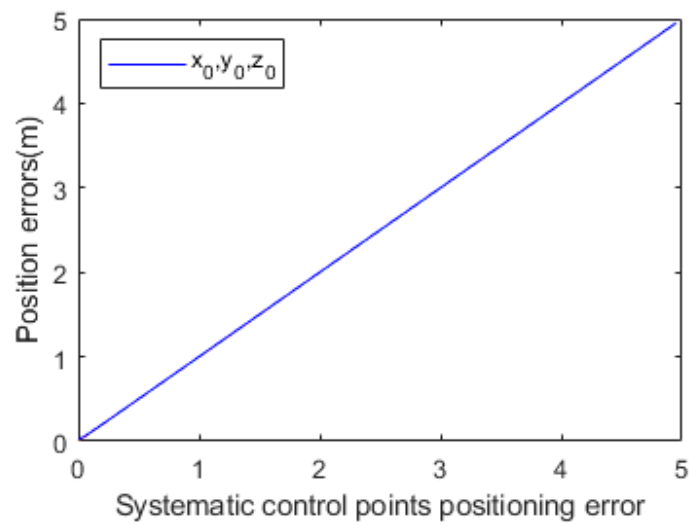


Figure 5. Systematic control points positioning error propagation curve.

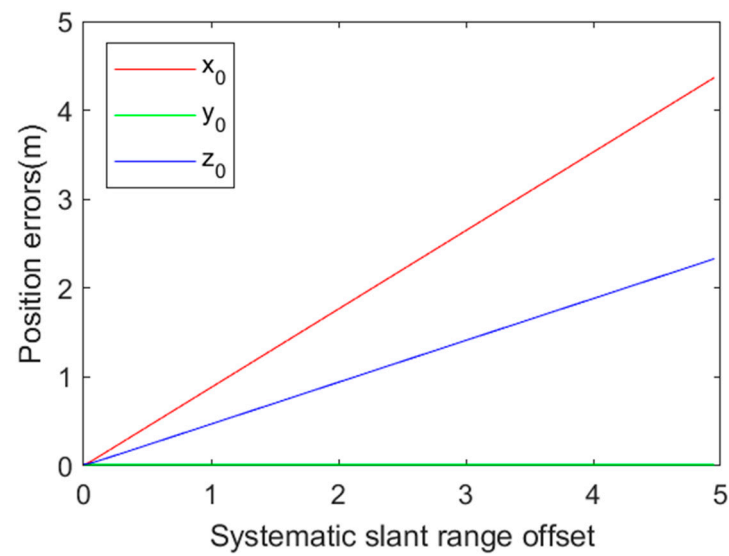


Figure 6. Systematic slant range error propagation curve.

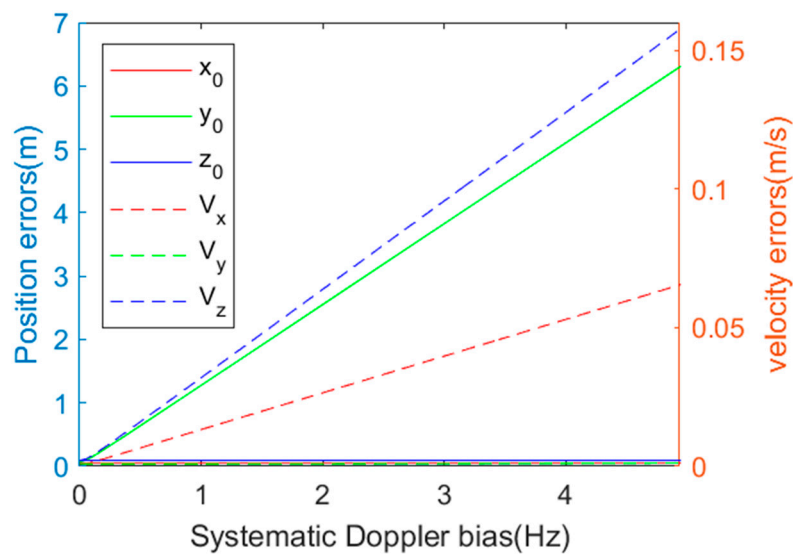


Figure 7. Doppler bias propagation curve.

In Figure 5, due to the same error propagation coefficient in Equation (33), the three-dimensional positioning error of the systematic control points introduces an equivalent positioning translation error in the three directions of the SAR platform position, and the three error propagation curves are the same straight line.

In Figure 6, the azimuth position y_0 is not affected by the systematic slant range error, while the range position x_0 is considerably affected, and the vertical position z_0 is affected the least.

In Figure 7, the positions of x_0, z_0, v_y are not affected by the Doppler bias, while the azimuth position y_0 , the vertical velocity v_z , and the range velocity v_x are considerably affected, while the others are hardly affected.

Figures 8 and 9 show the error propagation curves of random errors.

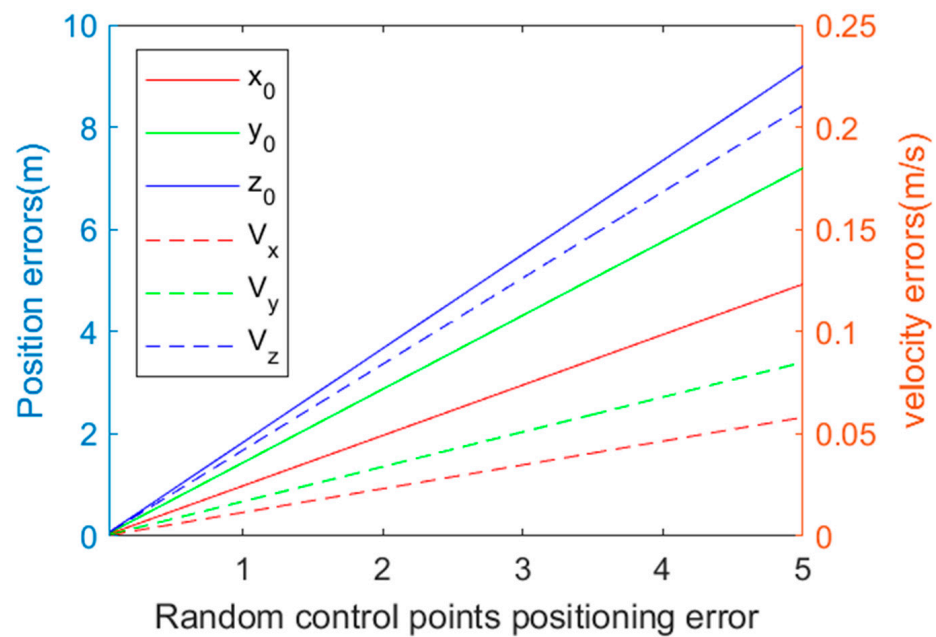


Figure 8. Random control points positioning error propagation curve.

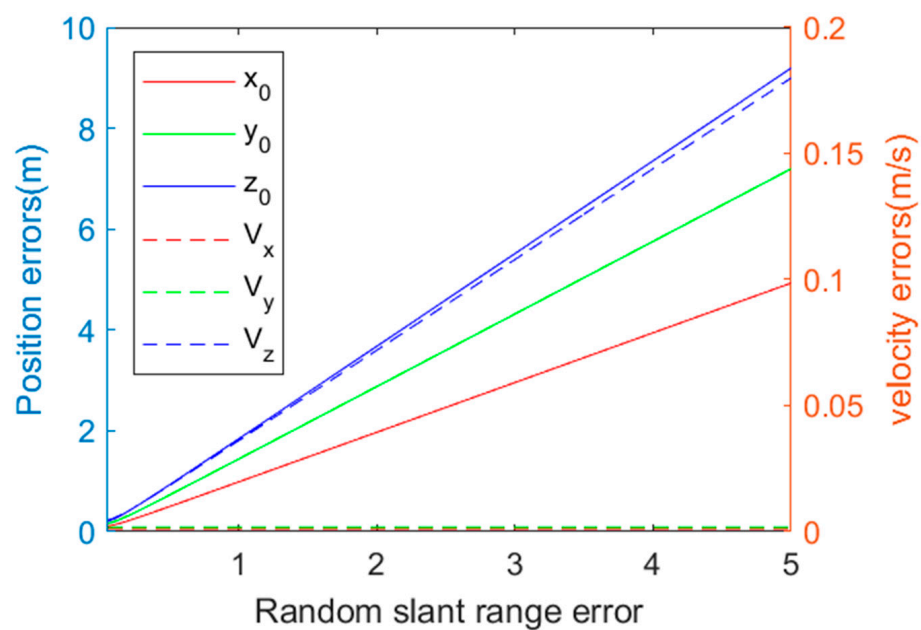


Figure 9. Random slant range error propagation curve.

It can be seen from Figure 8 that the random control points positioning error has different degrees of influence on the six parameters, with the greatest impact on the vertical position z_0 and velocity v_z .

According to Figure 9, the random slant range error affects the estimation of the three directions of position and the vertical velocity to varying degrees, and has little effect on the horizontal velocity.

4.2. System Parameter Effects on Positioning Error

When the SAR system operates under different imaging parameters, the same input error can result in different positioning errors. A single-factor analysis was conducted on two parameters, platform flight altitude and imaging center distance, to investigate their impacts on the positioning error. In the experiments in this section, the error settings in Table 2 were used.

Table 2. Simulation error settings.

Simulation Errors	Value
Systematic slant range offset	3 m
Systematic control points positioning error	3 m
Systematic Doppler bias	2 Hz
Random slant range error	2 m
Random control points positioning error	2 m

As shown in Figure 10, with the increase in the imaging center distance, the positioning errors in range and azimuth directions x_0, z_0 increase rapidly, while the y_0, v_x, v_y, v_z error increases relatively slowly.

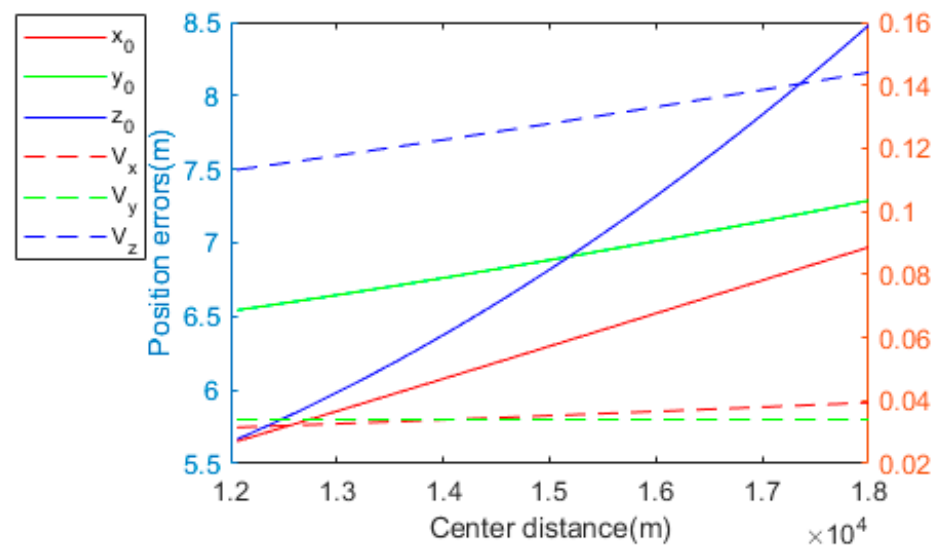


Figure 10. Curve of positioning error with respect to the center distance.

From Figure 11, when the platform flight altitude is increased, the vertical position z_0 and velocity v_z error decrease rapidly, while the range and azimuth position x_0, y_0 errors increase slightly. This indicates that appropriately increasing the platform altitude can improve the positioning accuracy.

By keeping the distribution of ground-control points unchanged and changing the number of control points, it can be seen from Figure 12 that the positioning errors of all parameters decrease rapidly at first and then tend to be flat in a similar pattern, indicating that appropriately increasing the number of control points can improve the positioning.

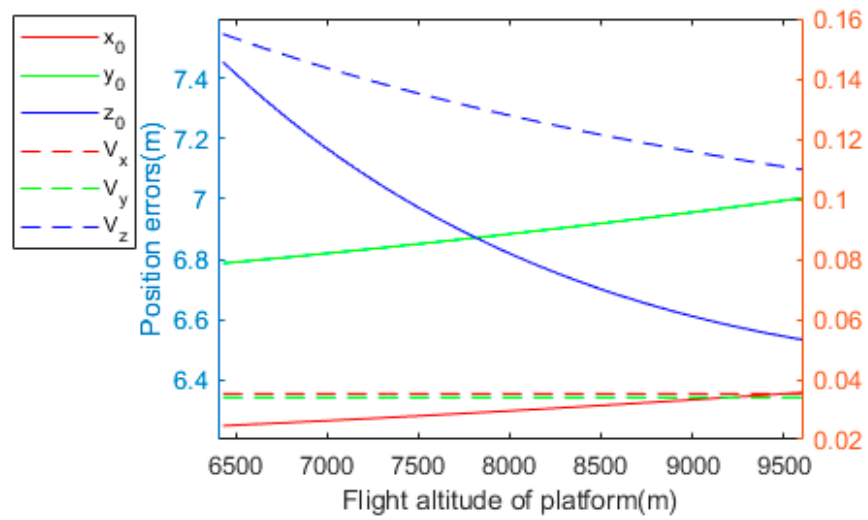


Figure 11. Curve of positioning error with respect to the flight altitude.

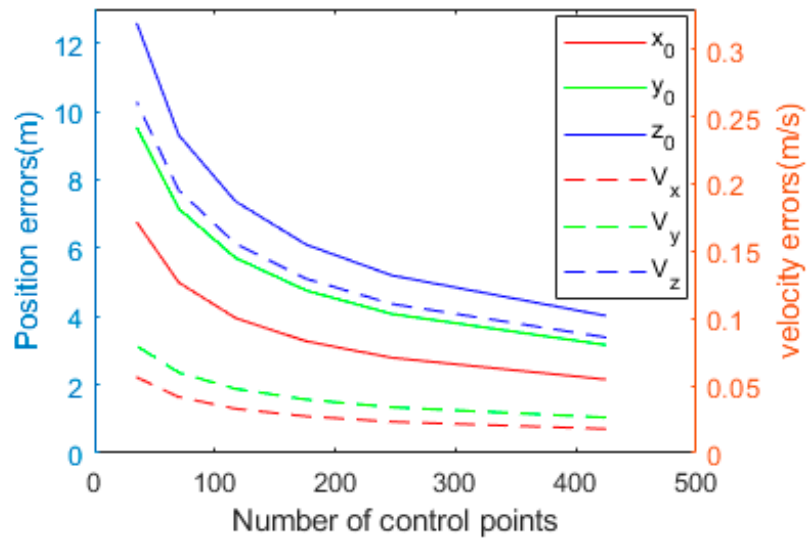


Figure 12. Curve of positioning error with respect to the number of control points.

4.3. Semi-Physical Simulation Verification

Actual SAR images were used for verification, as shown in Figure 13. The left half shows the SAR image used and the right half shows the corresponding optical reference image.

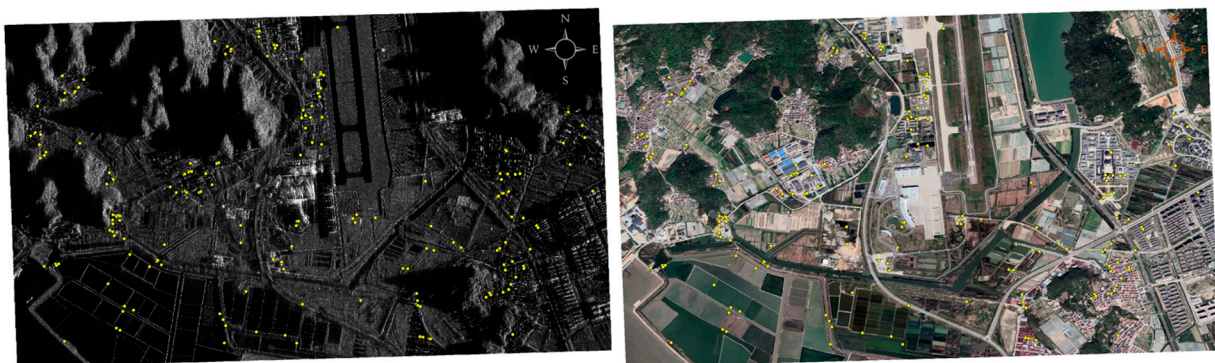


Figure 13. Actual SAR and corresponding optical images in the region of interest.

The SRAWG feature description method proposed by the author was used for heterogeneous image-matching [20]. The feature points of the image were evenly distributed in the image by block partitioning [21], and the matching accuracy could reach the pixel level by using a dense feature description. The yellow dots in the figure are the control points obtained after image-matching, and after obtaining the corresponding feature point pairs in the images, we transformed the SAR image to the geographic coordinate system using a bilinear interpolation, in order to obtain the geographical coordinates of the control points. The imaging parameters of the system are shown in Table 3, and the Scenarios of semi-physical simulation are shown in Figure 14.

Table 3. Semi-physical simulation system parameters.

Parameters	Value
Flight altitude of platform	4908.5 m
Center distance	34,196.9 m
Flight speed	51.8 m/s
Resolution	0.3 m
Imaging area	2905 m × 4404 m
Image size	11,200 × 14,336
Number of control points	200

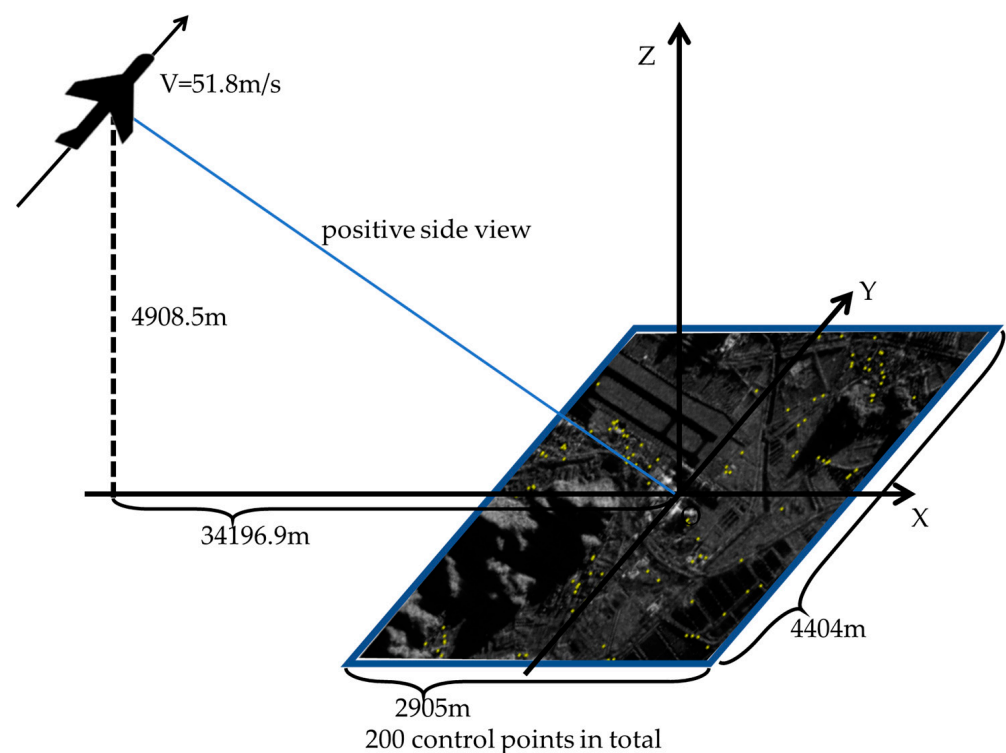


Figure 14. Scenarios of semi-physical simulation.

During the process of heterogeneous image-matching, it was necessary to register the images to the geographic coordinate system and establish the correspondence between the focused images and the geographical coordinates. In this process, we employed a bilinear interpolation.

The systematic offset and random error of each error source in the simulation were set as shown in Table 4.

Table 4. Semi-physical simulation error settings.

Simulation Errors	Value
Systematic slant range offset	3 m
Systematic control points positioning error	3 m
Systematic Doppler bias	2 Hz
Random slant range error	1 m
Random control points positioning error	1 m

If the platform state was directly solved using the range and Doppler equations, the solution could not converge due to the ill-posed problem of the equations. The three-step method proposed in this paper was applied to solve the platform position and velocity, and 1000 Monte-Carlo experiments were conducted to statistically analyze the error of the parameter estimation. The results were compared with the theoretical error analysis values shown in Tables 5–7. The theoretical error analysis model is described in Sections 3.1 and 3.2.

Table 5. Platform positioning error introduced by systematic errors.

Parameters	x_0 (m)	y_0 (m)	z_0 (m)	v_x (m/s)	v_y (m/s)	v_z (m/s)
Estimation errors	5.87	17.1	4.0	0.0296	0.0008	0.2080
Theoretical errors Δ	5.96	17.0	3.7	0.0296	0.0008	0.2115

Table 6. Platform Positioning Error Introduced by Random Errors.

Parameters	x_0 (m)	y_0 (m)	z_0 (m)	v_x (m/s)	v_y (m/s)	v_z (m/s)
Estimation errors	3.16	4.94	22.19	0.00321	0.00519	0.0571
Theoretical errors σ	3.20	4.86	22.46	0.00325	0.00512	0.0573

Table 7. Platform Positioning Error Introduced by the Combination of Two Types of Errors.

Parameters	x_0 (m)	y_0 (m)	z_0 (m)	v_x (m/s)	v_y (m/s)	v_z (m/s)
Estimation errors	6.51	17.64	22.54	0.0299	0.00526	0.213
Theoretical errors $\sqrt{\Delta^2 + \sigma^2}$	6.76	17.68	22.76	0.0297	0.00518	0.219

The experiment showed that this method could achieve robust and high-precision estimations of SAR platform motion parameters. Under the influence of typical systematic errors, the estimation accuracy of the distance position of the SAR platform was about 6.5 m, and the estimation accuracy of the azimuth position was about 17.6 m, most of which was affected by systematic errors. The estimation accuracy of the vertical position was about 22.5 m, which was more affected by random errors than by systematic errors. As for the velocity estimation accuracy, the estimation accuracy of the range velocity was better than 0.03 m/s, mainly affected by systematic errors. The estimation accuracy of the azimuth velocity was the highest, about 0.005 m/s, and the error mainly came from random errors. The estimation accuracy of the vertical velocity was slightly lower, about 0.2 m/s. Comparing the estimation error with the theoretical error predicted in Sections 3.1 and 3.2, the two were highly consistent, further verifying the effectiveness and accuracy of the error analysis model derived in this paper.

5. Discussion

Based on the theoretical analysis and experimental results, the estimation in the vertical direction was the most susceptible to random errors. In the curve of random control point position error and random slant distance error transmission, the derivatives of the vertical position and velocity curves were both maximum values. From the perspectives of

systematic and random errors, the former mainly affected horizontal positioning, while the latter mainly affected vertical positioning. From the perspective of system parameters, increasing the flight altitude and shortening detection distance were beneficial for improving positioning accuracy, especially in the vertical direction. In terms of control point selection, a certain number of high-reliability control points should be chosen instead of a large number of low-precision control points, as the benefits of increasing the control point quantity are diminishing. The abovementioned analysis was validated in the semi-physical simulation.

In the future work, we will construct a complete simulation model to integrate the platform positioning method into the entire process loop of navigation. We will attempt to assist INS navigation in the absence of GNSS, and further explore practical testing methods.

6. Conclusions

SAR image-matching-aided navigation is one of the future research focuses of airborne SAR systems based on the SAR imaging model. This paper established a motion model of the airborne SAR platform, fully utilized ground-position information, imaging slant range information, and Doppler frequency information to establish a nonlinear over-determined equation group. The singular value decomposition was used in the equation solution, and the equation was decoupled using the three-step method to achieve robust and high-precision estimations of platform motion parameters. The theoretical error analysis was then performed, and the theory was consistent with the simulation. The impact of systematic and random errors on positioning accuracy was analyzed. Finally, the validity of the positioning method and the accuracy of the error model were verified through a semi-physical simulation.

Author Contributions: All the authors made significant contributions to the work. W.T. and A.Y. conducted the experiment framework. W.T., A.Y. and K.Z. processed the experiment data; W.T. wrote the manuscript; W.T. and A.Y. analyzed the data; Z.D. provided insightful suggestions for the work and the manuscript. All authors have read and agreed to the published version of the manuscript.

Funding: This research received no external funding.

Data Availability Statement: The data presented in this study are available on request from the corresponding author.

Acknowledgments: The authors would like to thank all the anonymous reviewers for their valuable comments and helpful suggestions, which led to substantial improvements of this paper.

Conflicts of Interest: The authors declare no conflict of interest.

References

1. Moreira, A.; Hounam, D. Foreword to the special issue on synthetic aperture radar (sar) technologies and techniques. *IEEE Trans. Geosci. Remote Sens.* **2007**, *45*, 3303–3305. [[CrossRef](#)]
2. Seo, J.; Lee, J.G. Application of nonlinear smoothing to integrated GPS/INS navigation system. *J. Glob. Position. Syst.* **2005**, *4*, 88–94. [[CrossRef](#)]
3. Greco, M.; Querry, S.; Pinelli, G. SAR-based augmented integrity navigation architecture. In Proceedings of the 2012 13th International Radar Symposium, Warsaw, Poland, 9 July 2012. [[CrossRef](#)]
4. White, T.; Wheeler, J. Gps-Denied Navigation Using Sar Images and Neural Networks. In Proceedings of the ICASSP 2021—2021 IEEE International Conference on Acoustics, Speech and Signal Processing (ICASSP), Toronto, ON, Canada, 6 June 2021. [[CrossRef](#)]
5. Lu, J.; Ye, L. A deep fusion method based on ins/sar integrated navigation and sar bias estimation. *IEEE Sens. J.* **2020**, *20*, 10057–10070. [[CrossRef](#)]
6. Nitti; Davide, O. Feasibility of Using Synthetic Aperture Radar to Aid UAV Navigation. *Sensors* **2015**, *15*, 18334–18359. [[CrossRef](#)] [[PubMed](#)]
7. Qing, Y.; Li, H. Missile location based on SAR seeker. *Acta Electron. Sin.* **2009**, *31*, 121–124.
8. Qing, Y.; Huang, Z. Missile Geo-Location Using INS and Dual-Antenna Missile-Borne SAR. *Acta Electron. Sin.* **2009**, *37*, 1216–1221.
9. Fu, X. Study on the Technology of Scene Matching and Missile Location for Bistatic Missile-Borne SAR. Master's Thesis, University of Electronic Science and Technology of China, Chengdu, China, 2015.
10. Deng, H. Study on Imaging and Positioning of Missile-Borne Monostatic/Bistatic SAR with Curve Tracks. Ph.D. Thesis, Xidian University, Xi'an, China, 2018.

11. Li, Y.; Lan, J. Positioning of Missile with Terminal Guide SAR System and Analysis. *J. Telem. Track. Command.* **2004**, *25*, 29–33.
12. Li, Y.; Lv, X.L. Research on positioning and measuring speed in the high speed SAR system based on high precision map matching. *Syst. Eng. Electron.* **2007**, *29*, 1851–1855.
13. Chen, S.; Liu, X. SAR Positioning Method based on High-precision Scene Matching. *J. Natl. Univ. Def. Technol.* **2016**, *38*, 121–126.
14. Chen, S.; Liu, X. SAR Platform Location Method based on Scene Matching and Inertial Navigation System Information. *J. Natl. Univ. Def. Technol.* **2017**, *39*, 105–109.
15. Cheng, H.; Lu, W. SAR Platform Geo-location Based on Least Squares Support Vector Machines. *J. Astronaut.* **2010**, *31*, 489–494.
16. Toss, T.; Dämmert, P. Navigation with SAR and 3D-map aiding. In Proceedings of the 2015 18th International Conference on Information Fusion (Fusion), Washington, DC, USA, 14 October 2015.
17. Chen, J.; Li, W. Convergence of Gauss-Newton’s method and uniqueness of the solution. *Appl. Math. Comput.* **2005**, *170*, 686–705. [[CrossRef](#)]
18. Wu, J.; Li, M. Ill Matrix and Regularization Method in Surveying Data Processing. *J. Geod. Geodyn.* **2010**, *30*, 102–105.
19. An, T. Research on SAR/INS Intergraded Velocity and Position Measurement Technology. Master’s Thesis, National University of Defense Technology, Changsha, China, 2012.
20. Wang, Z.; Yu, A. A Fast Registration Method for Optical and SAR Images Based on SRAWG Feature Description. *Remote Sens.* **2022**, *14*, 5060. [[CrossRef](#)]
21. Wang, Z.; Yu, A. Performance Evaluation of Interest Point Detectors for Heterologous Image Matching. *Remote Sens.* **2022**, *14*, 724. [[CrossRef](#)]

Disclaimer/Publisher’s Note: The statements, opinions and data contained in all publications are solely those of the individual author(s) and contributor(s) and not of MDPI and/or the editor(s). MDPI and/or the editor(s) disclaim responsibility for any injury to people or property resulting from any ideas, methods, instructions or products referred to in the content.